ACS OMEGA

http://pubs.acs.org/journal/acsodf Article

Synthesis, Characterizations, and Electrochemical Performances of Highly Porous, Anhydrous $Co_{0.5}Ni_{0.5}C_2O_4$ for Pseudocapacitive Energy Storage Applications

Neeraj Kumar Mishra, Rakesh Mondal, Thandavarayan Maiyalagan, and Preetam Singh*

Cite This: *ACS Omega* 2022, 7, 1975−1987 Read Online

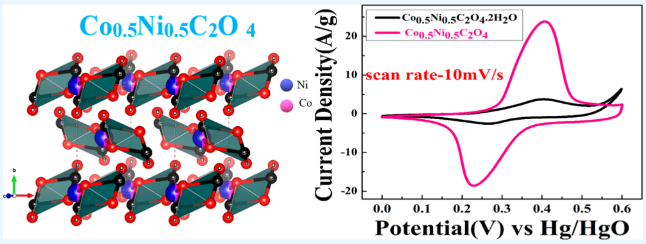

ABSTRACT: Electrochemical energy storage relies essentially on the development of innovative electrode materials with enhanced kinetics of ion transport. Pseudocapacitors are excellent candidates to bridge the performance gap between supercapacitors and batteries. Highly porous, anhydrous $Ni_{0.5}Co_{0.5}C_2O_4$ is envisaged here as a potential electrode for pseudocapacitor applications, mainly because of its open pore framework structure, which poses inherent structural stability due to the presence of planar oxalate anions ($C_2O_4^{2-}$), and active participation of $Ni^{2+/3+}$ and $Co^{2+/3+}$ results in high intercalative charge storage capacity in the aqueous KOH electrolyte. The $Ni_{0.5}Co_{0.5}C_2O_4$ electrode shows specific capacitance equivalent to 2396 F/g at 1 A/g in the potential window of 0.6 V in the aqueous 2 M KOH electrolyte by galvanostatic charge/discharge experiments. Predominant pseudocapacitive mechanism seems to operative behind high charge storage due to active participation of $Ni^{2+/3+}$ and $Co^{2+/3+}$ redox couple as intercalative (inner) and surface (outer) charges stored by porous anhydrous $Co_{0.5}Ni_{0.5}C_2O_4$ were close to high 38 and 62% respectively. Further, in full cell asymmetric supercapacitors (ASCs) in which porous anhydrous $Co_{0.5}Ni_{0.5}C_2O_4$ was used as the positive electrode and activated carbon (AC) was utilized as the negative electrode, in the operating potential window 1.6 V, the highest specific energy of 283 W h/kg and specific power of ~817 W/kg were achieved at 1 A/g current rates. Even at a very high power density of 7981 W/kg, the hybrid supercapacitor still attains an energy density of ~75 W h/kg with high cyclic stability at a 10 A/g current rate. The detailed electrochemical studies confirm higher cyclic stability and a superior electrochemical energy storage property of porous anhydrous $Co_{0.5}Ni_{0.5}C_2O_4$, making it a potential pseudocapacitive electrode for large energy storage applications.

■ INTRODUCTION

Uninterrupted fuel and power supply is a driving force for the innovations and growth of mankind to sustain modern civilization, and continuous depletion of natural sources of fossil fuels and associated environmental concerns has boosted the demand for sustainable, clean, and green energy generation.[1] Various classes of cleaner energy sources such as wind energy, solar power, and sea tides were explored, and continuous and controlled supply of energy from these sources requires the development and growth of devices meant for energy conversion and storage.[2] Electrochemical energy storage is the most suitable technology for energy conversion and storage due to high theoretical efficiency of converting chemical energy to electrical energy.[3] The energy storage process at electrode surfaces involves different phenomena due to the distinctive nature of the electrode and electrolyte interactions. Generally, three types of interaction occur on the electrode surface between the electrode and electrolyte known as (1) EDLC, (2) surface redox, and (3) intercalation of ions.[4] Surface redox and intercalation are followed by the faradic law because of charge transformation reaction involved in the energy storage mechanism.[5] Surface absorption, surface redox, and intercalation are responsible for pseudocapacitance and involve thermodynamic and kinetic behavior of electrosorption/desorption.[6,7] Interaction of species on the electrode surface is via either attraction or repulsion; surface attraction (redox) is followed by Langmuir electrosorption (sharp peak in the cyclic voltammetry curve) and repulsion (peak broadening) is followed by Frumkin electrosorption (broad peak in the cyclic voltammetry curve).[8] RuO_2 was the first reported material to show pseudocapacitive charge storage behavior.[9] $MnO_2 \cdot xH_2O$ performed as a capacitor in a neutral electrolyte.[10] According to the charge storage mechanism, pseudocapacitors have access to different oxidation states for redox charge transfer that can enable higher energy density compared

Received: October 1, 2021
Accepted: December 14, 2021
Published: January 4, 2022

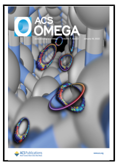

https://doi.org/10.1021/acsomega.1c05356

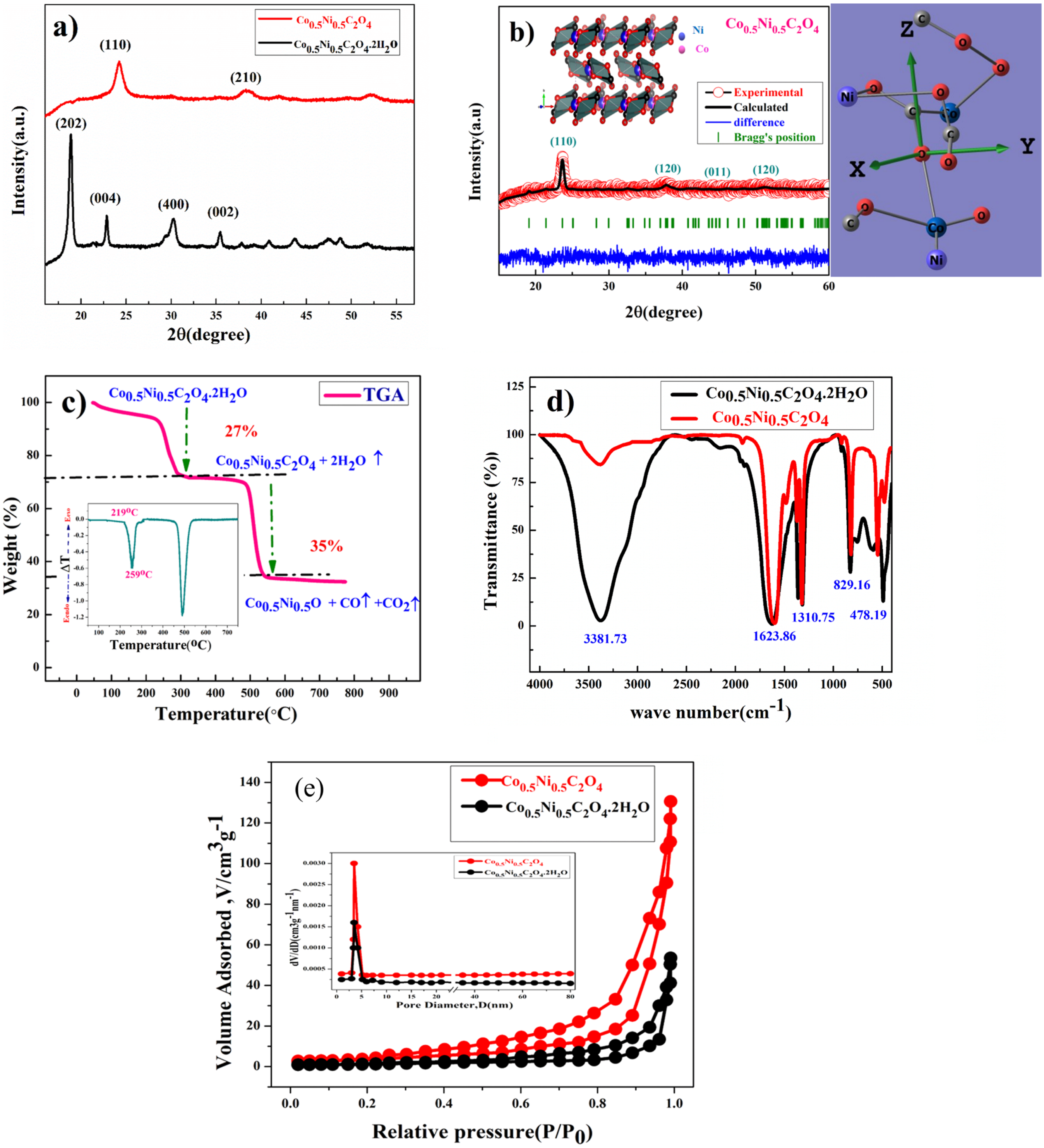

Figure 1. (a) XRD pattern of $Ni_{0.5}Co_{0.5}C_2O_4{\cdot}2H_2O$ and $Ni_{0.5}Co_{0.5}C_2O_4$, (b) Rietveld refinement of the XRD profile of anhydrous $Ni_{0.5}Co_{0.5}C_2O_4$ (vista image in the inset), (c) TGA of $Ni_{0.5}Co_{0.5}C_2O_4{\cdot}2H_2O$ in a N_2 atmosphere (inset shows the DTA plot), (d) FT-IR spectra of $Ni_{0.5}Co_{0.5}C_2O_4{\cdot}2H_2O$ and $Ni_{0.5}Co_{0.5}C_2O_4$, and € BET surface area measurement plot of $Ni_{0.5}Co_{0.5}C_2O_4{\cdot}2H_2O$ and $Ni_{0.5}Co_{0.5}C_2O_4$.

to EDLC.[11,12] To increase higher energy density, an asymmetry cell shows better performance when the capacitor component stores electrochemical energy by electrostatic force, and the battery component enhances the electron transfer in the hybrid electrode system, which leads to better charge transfer reaction at high current rates.[13] Many studies are being carried out on transition metal oxide-based materials such as NiO, V_2O_5, spinel Co_3O_4, Fe_2O_3, and mixed spinel $NiCo_2O_4$ to explore electrodes for the pseudocapacitor.[14−20] However, structural instability and performance degradation issues related to transition metal oxide lead to investigation of the novel framework structure for higher surface charge storage and better structural stability.[21−23] Metal−organic frameworks (MOFs) are used as an interesting open framework structure, where materials are constructed by joining metal-containing units with organic linkers, generating an interesting threedimensional or two-dimensional network with permanent porosity.[24] Highly porous metal−organic framework structures, especially utilizing an oxalate linker with active participation metal ion redox, are known to show faradic pseudocapacitive characteristics.[25−27] However, most of the oxalate materials have a high open structural space to accommodate the hydration of water, and that is why, most of the transition metal oxalates contain a structural water molecule. We have envisaged the controlled removal of structural water from the material to develop a novel porous structure that can accommodate a high degree of charge or anion intercalation/deintercalation couple with double layer capacitance to achieve superior capacitance.[22b] The controlled water removal can maintain the high porosity of the structure that can enable fast charge/ion transfer.

Here, in this article, we present the synthesis, characterizations, and electrochemical performances of hydrated $Co_{0.5}Ni_{0.5}C_2O_4{\cdot}2H_2O$ and porous anhydrous $Co_{0.5}Ni_{0.5}C_2O_4$ electrodes. The porous anhydrous $Co_{0.5}Ni_{0.5}C_2O_4$ electrode shows the specific capacitance value of 2396 F/g at 1 A/g, whereas hydrated $Co_{0.5}Ni_{0.5}C_2O_4{\cdot}2H_2O$ shows the capacitance equivalent to 810 F/g at 1 A/g in an aqueous 2 M KOH electrolyte. Furthermore, we assembled aqueous asymmetric supercapacitors (ASCs), in which porous anhydrous $Co_{0.5}Ni_{0.5}CO_4$ was used as the positive electrode and activated carbon (AC) was utilized as the negative electrode. Highest specific energy equivalent to 283 W h/kg and specific power of ∼817 W/kg were achieved at 1 A/g current rates by the combination of porous anhydrous $Co_{0.5}Ni_{0.5}C_2O_4$ and AC with high cyclic stability.

EXPERIMENTAL SECTION

Synthesis. Synthesis of $Co_{0.5}Ni_{0.5}C_2O_4{\cdot}2H_2O$ was carried out by the precipitation method. Highly porous anhydrous $Co_{0.5}Ni_{0.5}CO_4$ was prepared in two step synthesis. 1.49 g of cobolt(II) nitrate hexahydrate ($Co(NO_3)_2{\cdot}6H_2O$) and 1.46 g of nickel(II) nitrate hexahydrate ($Ni(NO_3)_2{\cdot}6H_2O$) were dissolved in 200 mL of deionized water with continuous stirring using a hot plate magnetic stirrer, and 1.27 g of oxalic acid dehydrate ($H_2C_2O_4{\cdot}2H_2O$) was added in solution. The entire mixture was stirred vigorously at 80 °C for 5 h. After 5 h of stirring, a white color precipitate of product $Co_{0.5}Ni_{0.5}C_2O_4{\cdot}2H_2O$ was obtained. The obtained product is then washed several times with deionized water. Finally, the washed product, $Co_{0.5}Ni_{0.5}C_2O_4{\cdot}2H_2O$, was dried in a hot air oven at 90 °C for overnight. Porous anhydrous $Co_{0.5}Ni_{0.5}C_2O_4$ was formed after heating the material at 230 °C for 5 h in a N_2 atmosphere.

$$\begin{aligned}&Co(NO_3)_2{\cdot}6H_2O + Ni(NO_3)_2{\cdot}6H_2O\\&\quad + 2H_2C_2O_4{\cdot}2H_2O\\&\quad \rightarrow 2Co_{0.5}Ni_{0.5}C_2O_4{\cdot}2H_2O\downarrow + 2HNO_3 + 4H_2O \text{ at}\\&\quad 80\ ^{\circ}C\end{aligned} \tag{1}$$

$$\begin{aligned}&Co_{0.5}Ni_{0.5}C_2O_4{\cdot}2H_2O\\&\quad \rightarrow Co_{0.5}Ni_{0.5}CO_4 + 2H_2O\uparrow \text{ at } 230\ ^{\circ}C\end{aligned} \tag{2}$$

Characterizations. The crystal structure and phase purity of synthesized products were characterized through a Rigaku Miniflex desktop X-ray diffractometer (XRD) with Cu-Ka radiation (λ = 0.154 nm) in the range of 2θ = 10−90° with a step size of 0.02°. Xpert High Score (PANanalytical) software was used to identify the required phase. FE-SEM (FP 5022/22) was used to determine the surface morphology and structure of the sample. Infrared spectra of the samples were recorded using a Nicolet iS5 FTIR spectrometer in the range of 400−4000 cm^{-1}. Pore size distribution and specific surface area of the sample were measured by BET (MicrotracBEL). All electrochemical performances of the sample including cyclic voltammetry (CV), galvanostatic charge discharge (GCD), and electrochemical impedance spectroscopy (EIS) were conducted using a conventional three-electrode arrangement measured by Metrohm Autolab (PGSTAT204) equipped with a FRA32M module. Electrochemical measurements were analyzed using NOVA1.1 software.

Preparation of Electrode. Hydrated $Co_{0.5}Ni_{0.5}C_2O_4{\cdot}2H_2O$ and anhydrous porous $Co_{0.5}Ni_{0.5}C_2O_4$ working electrodes were prepared in a 7:2:1 ratio of the active material, activated carbon, and binder (PVDF) in NMP solvent. Homogenous slurry was prepared using a mortar, and slurry containing ∼1 mg of active materials was cast over a 1 cm^2 area of Toray carbon paper. The coated electrode was dried at 80 °C for 12 h. The electrode loading was calculated through taking the weight of the electrode using an electronic balance (error limit: 0.01 mg). For that, the weight of Torrey paper was taken first, and then, the weight of the coated electrode (after drying the coated ink on Torrey carbon paper on 1 × 1 cm^2 area) was taken for the study. Then, from the difference in the weight, the exact loading of the electrode material was calculated.

RESULTS AND DISCUSSION

The XRD peak pattern of $Co_{0.5}Ni_{0.5}C_2O_4{\cdot}2H_2O$ and anhydrous $Co_{0.5}Ni_{0.5}C_2O_4$ powder confirms the phase purity and formation of the single phase material. Figure 1a shows the XRD plot of $Co_{0.5}Ni_{0.5}C_2O_4{\cdot}2H_2O$ and anhydrous $Co_{0.5}Ni_{0.5}C_2O_4$ in the 2θ range of 10−60° with a step size of 0.02°. The prominent sharp diffraction peaks at 18.84, 22.78, 30.35, 35.6, and 49.08 represent the (202), (004), (400), (022), and (602) planes of $Co_{0.5}Ni_{0.5}C_2O_4{\cdot}2H_2O$ in the orthorhombic cell (space group: *Cccm*) and matches very well with the diffraction pattern of $NiC_2O_4{\cdot}2H_2O$ (JCPDS no. 25-0582).[28,29] After annealing at 230 °C for 5 h, $Co_{0.5}Ni_{0.5}C_2O_4.2H_2O$ transformed into anhydrous $Co_{0.5}Ni_{0.5}C_2O_4$ in the α-monoclinic structure (space group *P*21/*n*, JCPDS no.: 37-0719). Figure 1b shows the Rietveld Refined XRD profile of $Co_{0.5}Ni_{0.5}C_2O_4$ with lattice parameters a = 5.23400 Å, b = 5.653000 Å, c = 7.15900 Å, α-90°, β-118.88°, and γ-90°, and the VESTA image is shown in the inset.[30]

Thermogravimetric analysis (TGA) as shown in Figure 1c was used to understand the thermal stability of $Co_{0.5}Ni_{0.5}C_2O_4{\cdot}2H_2O$. The first weight loss occurred at the temperature from 100 to 300 °C, which corresponds to the removal of structural water from the sample; in this temperature range, phase transformation also occurred from orthorhombic to monoclinic. The TGA curve determines the weight loss of 27%, as 2 mol of water was removed from the sample in the temperature range of 100−300 °C. DTA shown in the inset clearly shows structure water leaving the structure at 219 °C, and the second weight loss step or decomposition of the oxalate group occurs in the temperature range of 350−500 °C, in which the weight loss of 35% was observed for decomposition of $Co_{0.5}Ni_{0.5}C_2O_4$. That is why, to perform the control dehydration of materials,

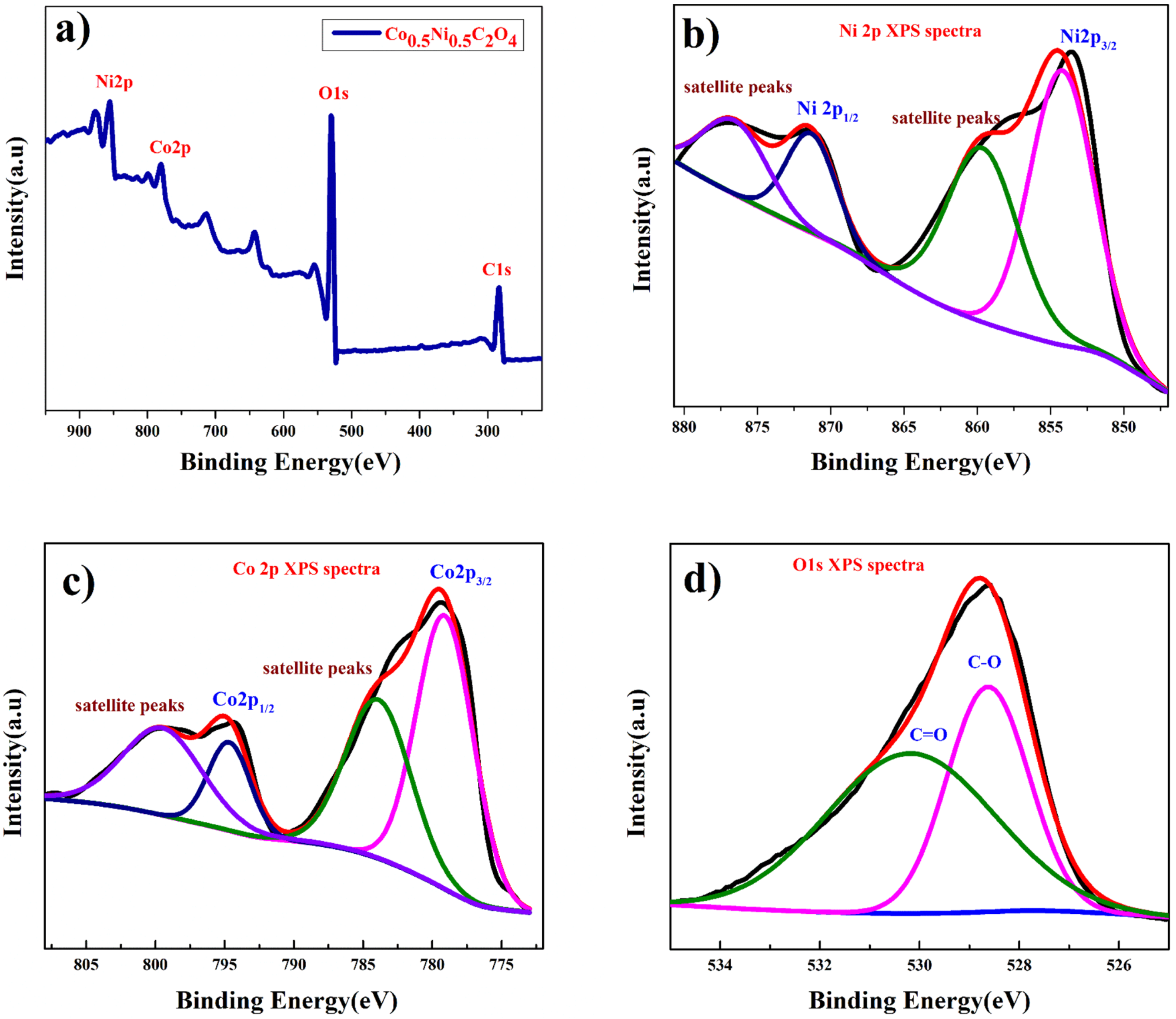

Figure 2. XPS plot of (a) full survey $Ni_{0.5}Co_{0.5}C_2O_4$, (b) Ni (2p) spectra, (c) Co 2p spectra, and (d) O (1s) spectra.

we carried out dehydration or annealing at 230 °C to avoid rapid loss of structure water that can damage the porous structure and can result in particle segregation. Thus, to protect the porous structure of the anhydrated materials, annealing was carried out at 230 °C in a N_2 atmosphere. Weight loss steps can be represented as follows

$$Co_{0.5}Ni_{0.5}C_2O_4\cdot 2H_2O \rightarrow Co_{0.5}Ni_{0.5}C_2O_4 + 2H_2O\ (\text{above } T \sim 200\ °\text{C}) \tag{3}$$

$$Co_{0.5}Ni_{0.5}C_2O_4 \rightarrow Co_{0.5}Ni_{0.5}O + CO + CO_2\ (T \geq 450\ °\text{C}) \tag{4}$$

FTIR spectra of $Co_{0.5}Ni_{0.5}CO_4\cdot 2H_2O$ and anhydrous $Co_{0.5}Ni_{0.5}CO_4$ powder samples shown in Figure 1d reveal the presence of different functional groups in the material. The broad peak at 3381.71 cm^{-1} belongs to the stretching vibration of the hydroxyl group (−OH), which signifies the presence of water in $Co_{0.5}Ni_{0.5}CO_4\cdot 2H_2O$. The observed peak at 1620.75 cm^{-1} was assigned to the antisymmetric carbonyl stretching band (C═O) specific to the oxalate group.[30] Two weak peaks at 1326.86 and 1310.75 cm^{-1} were attributed to vibrations of $C_2O_4^{2-}$ (C−O) + (C−C) and (C−O) + (O−C═O), respectively. The peak at 829.16 cm^{-1} was assigned to the vibration mode of $C_2O_4^{2-}$ and O−C═O bending vibrations (O−C═O). The absorption peak at 478.19 cm^{-1} can be attributed to both Ni−O and Co−O bonding present in the prepared sample of Cobalt oxalate dehydrate ($Co_{0.5}Ni_{0.5}C_2O_4\cdot 2H_2O$). The annealing product after structural water removal represents $Co_{0.5}Ni_{0.5}C_2O_4$. The FT-IR study clearly shows the distinctive decrease in peak intensity of stretching vibration of the hydroxyl group (−OH) near 3381.73 cm^{-1}.[27] Figure 1e shows the BET results of the $Co_{0.5}Ni_{0.5}C_2O_4$ sample. The nitrogen adsorption and desorption isotherm shows characteristics, which corresponds to the mesoporous structure of the oxalate; $Co_{0.5}Ni_{0.5}C_2O_4$ sample. The calculated BET specific surface area and average pore diameter is 129.82 cm^2/g and both micropores and mesopores with diameters of 1.5−3.92 nm, respectively. Mesoporous structures attribute to excellent electrochemical kinetics due to high porosity. The calculated pore diameter of the $Co_{0.5}Ni_{0.5}C_2O_4$ sample is much higher than that of the ions present in aqueous electrolytes.[28,29]

Figure 2a shows the X-ray photoelectron spectroscopy (XPS) survey plot of the $Co_{0.5}Ni_{0.5}C_2O_4$ sample, further confirming the presence of Ni and Co in the material. The Ni (2p) spectrum shown in Figure 2b could be assigned to $2p_{3/2}$ of Ni^{2+} (854.12 eV) and $2p_{1/2}$ of Ni^{2+} (871.71 eV) ions, as well as the corresponding satellite peaks at 859.83 and 876.71 eV. The Co(2p) spectrum shown in Figure 2c could be divided into peaks, which can be assigned to $2p_{3/2}$ of Co^{2+} (779.11 eV) and $2p_{1/2}$ of Co^{2+} (794.81 eV) ions, as well as the corresponding satellite peaks at 783.87 and 799.87 eV that arise from Co^{2+} ions. The O(1s) spectra shown in Figure 2d represent two binding energies at 530.23 and 528.58 eV for different C=O and C−O bond stretchings.[30]

The SEM image shown in Figure 3a displays the particle distribution and morphology of the $Co_{0.5}Ni_{0.5}C_2O_4$ powder sample. Its shows spongy-like arrangement. The inset (energy-dispersive X-ray analysis) image represents the elemental analysis of anhydrous $Co_{0.5}Ni_{0.5}C_2O_4$. To determine the diameter of grains, imageJ software was used. Agglomerated sub-micron size grains are visible in the SEM image. TEM shows atomic arrangements at localized regions within the sample shown in Figure 3b. The inset image represents FFT (fast Furrier transformation) and inverse FFT, and the calculated *d* spacing was found to be 0.227 nm, which matches the (110) plane of $Co_{0.5}Ni_{0.5}C_2O_4$.

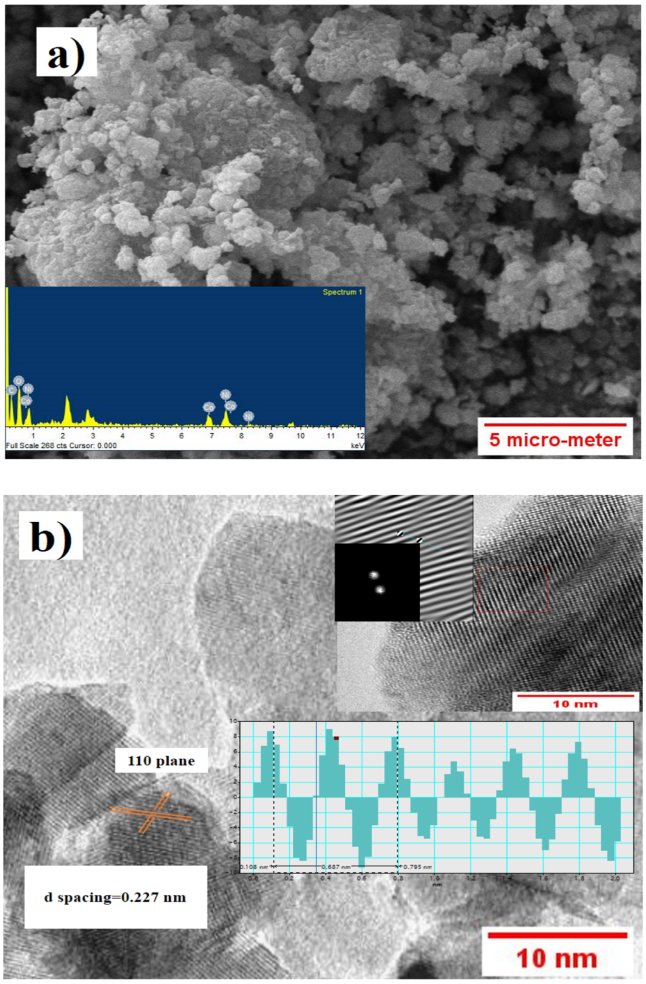

Figure 3. (a) SEM image showing morphology and particle size distribution of anhydrous $Ni_{0.5}Co_{0.5}$ C_2O_4 powder; inset shows the EDX image of anhydrous $Ni_{0.5}Co$ $_{0.5}C_2O_4$. (b) TEM image at localized regions; inset shows enlarged lattice fringes (with FFT and inverse FFT) and also (110) plane d spacing of porous anhydrous $Ni_{0.5}Co_{0.5}$ C_2O_4.

Electrochemical Studies. Electrochemical performance of $Co_{0.5}Ni_{0.5}C_2O_4{\cdot}2H_2O$ and porous anhydrous $Co_{0.5}Ni_{0.5}C_2O_4$ as the working electrode was characterized using a three-electrode system, where $Co_{0.5}Ni_{0.5}C_2O_4{\cdot}2H_2O$ and porous anhydrous $Co_{0.5}Ni_{0.5}C_2O_4$ act as working electrodes, saturated Hg/HgO (1 M KOH) as a reference electrode, and a platinum wire as a counter electrode in 2 M KOH as an electrolyte. The charge storage behavior of $Co_{0.5}Ni_{0.5}C_2O_4{\cdot}2H_2O$ and porous anhydrous $Co_{0.5}Ni_{0.5}C_2O_4$ was characterized using cyclic voltammetry (CV) curves in the potential range of 0−0.6 V. Figure 4a represents the CV curve of $Co_{0.5}Ni_{0.5}C_2O_4{\cdot}2H_2O$. The nature of the curve explains the pseudocapacitive behavior coupled with surface redox (electrosorption). The CV curve of highly porous anhydrous $Co_{0.5}Ni_{0.5}C_2O_4$ shown in Figure 4b shows that pseudocapacitive storage followed intercalative association with surface redox.[31] Redox peaks are originated due to the reversible transformation between Co^{2+} to Co^{3+} and Ni^{2+} to Ni^{3+} through electrosorption (redox) of OH^- ions.[31]

$$2Co_{0.5}(II)Ni_{0.5}(II)C_2O_4 + 2OH^-_{so} \leftrightarrow Ni_{0.5}(III)(OH^-)Co_{0.5}(III)(OH^-)C_2O_4 + 2e^- \quad (5)$$

From the CV curve, specific capacitance *C* (F/g) can also be calculated as one of the significant parameters to understand the electrochemical performance of the working electrode.[32]

$$C_{sp} = \frac{\int i\,(V)\mathrm{d}V}{mV\vartheta} \quad (6)$$

where "*m*" is the mass of active material in the electrode (g), "*V*" is the potential window (V), and "ϑ" is the scan rate (mV/s).

The specific capacitances of $Co_{0.5}Ni_{0.5}C_2O_4{\cdot}2H_2O$ and anhydrous $Co_{0.5}Ni_{0.5}C_2O_4$ were calculated using eq 6, and capacitance was found to be close to 671 and 1993 F/g at 1 mV/s, respectively. The highly porous anhydrous $Co_{0.5}Ni_{0.5}C_2O_4$ attains higher charge storage, resulting in much higher capacity compared to hydrated $Co_{0.5}Ni_{0.5}C_2O_4{\cdot}2H_2O$. In the voltage window of 0.6 V, the theoretical capacity of $Co_{0.5}Ni_{0.5}C_2O_4{\cdot}2H_2O$ and anhydrous $Co_{0.5}Ni_{0.5}C_2O_4$ will be 879.55 F/g and 1096 F/g, respectively, with $1e^-/OH^-$ charge transfer coupled with reversible intercalation/de-intercalation of OH^- ions. This suggests that there is at least transfer/exchange of $0/76e^-/OH^-$ per $Co_{0.5}Ni_{0.5}C_2O_4{\cdot}2H_2O$ and 1.82 e^-/OH^- per $Co_{0.5}Ni_{0.5}C_2O_4$ molecule, suggesting participation of both $Ni^{2+/3+}$ and $Co^{2+/3+}$ redox couples in charge storage. The redox reaction for high capacitance of $Co_{0.5}Ni_{0.5}C_2O_4{\cdot}2H_2O$ can be represented as

$$Co^{2+}_{0.5}Ni^{2+}_{0.5}C_2O_4{\cdot}2H_2O + 0.76OH^- \leftrightarrow Co^{3+}_{0.38}Co^{2+}_{0.12}Ni^{3+}_{0.38}Ni^{2+}_{0.12}C_2O_4{\cdot}2H_2O(OH^-)_{0.76} \quad (7)$$

As given in eq 8, the capacitance of $Co_{0.5}Ni_{0.5}C_2O_4$ can be represented as a combination of redox reaction as well as double layer formation as electron transfer is more than 1.

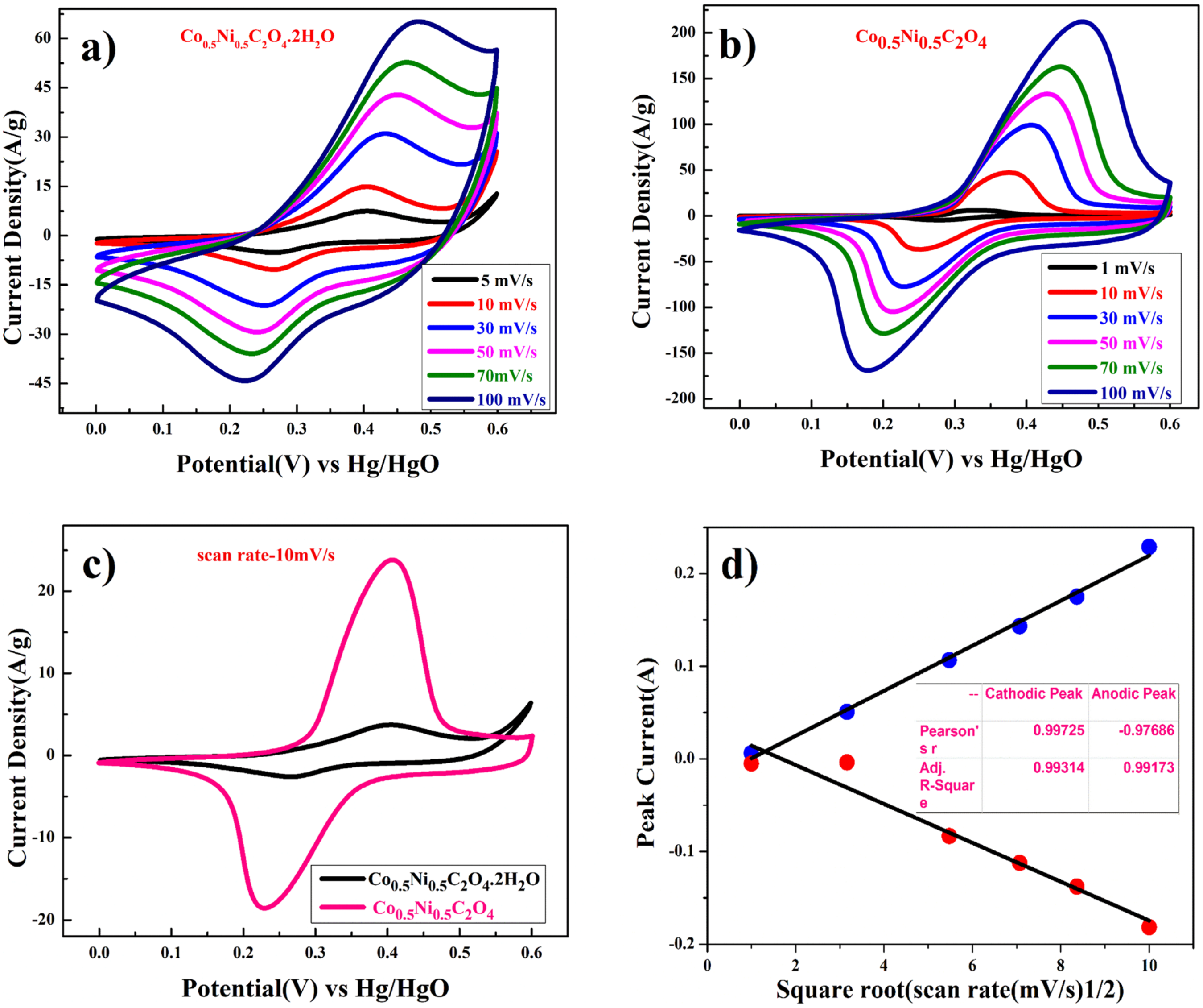

Figure 4. (a) Cyclic voltammetry of $Ni_{0.5}Co_{0.5}C_2O_4 \cdot 2H_2O$, (b) cyclic voltammetry of porous anhydrous $Ni_{0.5}Co_{0.5}C_2O_4$, (c) comparative cyclic voltammetry curves for $Ni_{0.5}Co_{0.5}C_2O_4 \cdot 2H_2O$ and $Ni_{0.5}Co_{0.5}C_2O_4$ electrodes at 10 mV/s, and (d) plot of log (peak current vs square root of the scan rate for porous anhydrous $Ni_{0.5}Co_{0.5}C_2O_4$).

$$Co^{2+}_{0.5}Ni^{2+}_{0.5}C_2O_4 + xOH^- + 1.82 - xKOH \leftrightarrow K^+_{1.82-x}Co^{2+}_{0.5-x}Co^{3+}_{x}N2^{3+}_{0.5-x}Ni^{3+}_{x}C_2O_4(OH^-)_{1.82} \quad (8)$$

The value of x can vary with scan rates, and the detailed electrochemistry $Co_{0.5}Ni_{0.5}C_2O_4$ is described later to understand the charge storage mechanism of the electrode. We believe that as $Co_{0.5}Ni_{0.5}C_2O_4$ can easily accommodate two structural water molecule to form $Co_{0.5}Ni_{0.5}C_2O_4 \cdot 2H_2O$, the anhydrous $Co_{0.5}Ni_{0.5}C_2O_4$ accommodate high charge transfer ($1.82e^-/OH^-$) coupled with double layer capacitance formation to result in very high capacity for the anhydrous $Co_{0.5}Ni_{0.5}C_2O_4$ electrode. Figure 4c shows a comparative plot of the CV curve of $Co_{0.5}Ni_{0.5}C_2O_4 \cdot 2H_2O$ and $Co_{0.5}Ni_{0.5}C_2O_4$ at a scan rate of 10 mV/s. The plot clearly reveals that there are two different types of redox phenomena occurring in the charge storage process; $Co_{0.5}Ni_{0.5}C_2O_4 \cdot 2H_2O$ follows surface redox and $Co_{0.5}Ni_{0.5}C_2O_4$ surface redox with intercalation and double layer formation.[33]

As the anhydrous $Co_{0.5}Ni_{0.5}CO_4$ electrode showed much superior pseudocapacitive storage, we focused our study mainly on the anhydrous $Co_{0.5}Ni_{0.5}CO_4$ only. Figure 4d shows the linear relation between anodic and cathodic peak current with respect to square root of scan rate and indicates that anhydrous $Co_{0.5}Ni_{0.5}CO_4$ undergoes the semi-infinite diffusion-controlled process. Furthermore, kinetics of the electrode can be understood by determining the diffusion coefficient. The diffusion coefficient for the electrode was determined using the Randles−Sevick equation.[34]

$$i_p = 2.686 \times 10^5 \times n^{3/2} A D^{1/2} C_o \nu^{1/2} \quad (9)$$

where i_p is peak current (A), n is the number of electrons transferred in the redox event (usually 1), A is the electrode area in cm^2, D is the diffusion coefficient in cm^2/s, C_o is the OH^- ion concentration in mol/cm^3, and ν is the scan rate in V/s. According to the equation, the diffusion coefficient of $Co_{0.5}Ni_{0.5}C_2O_4$ were calculated to be 1.916×10^{-11} cm^2/s for oxidation and 4.8931×10^{-11} cm^2/s for reduction.

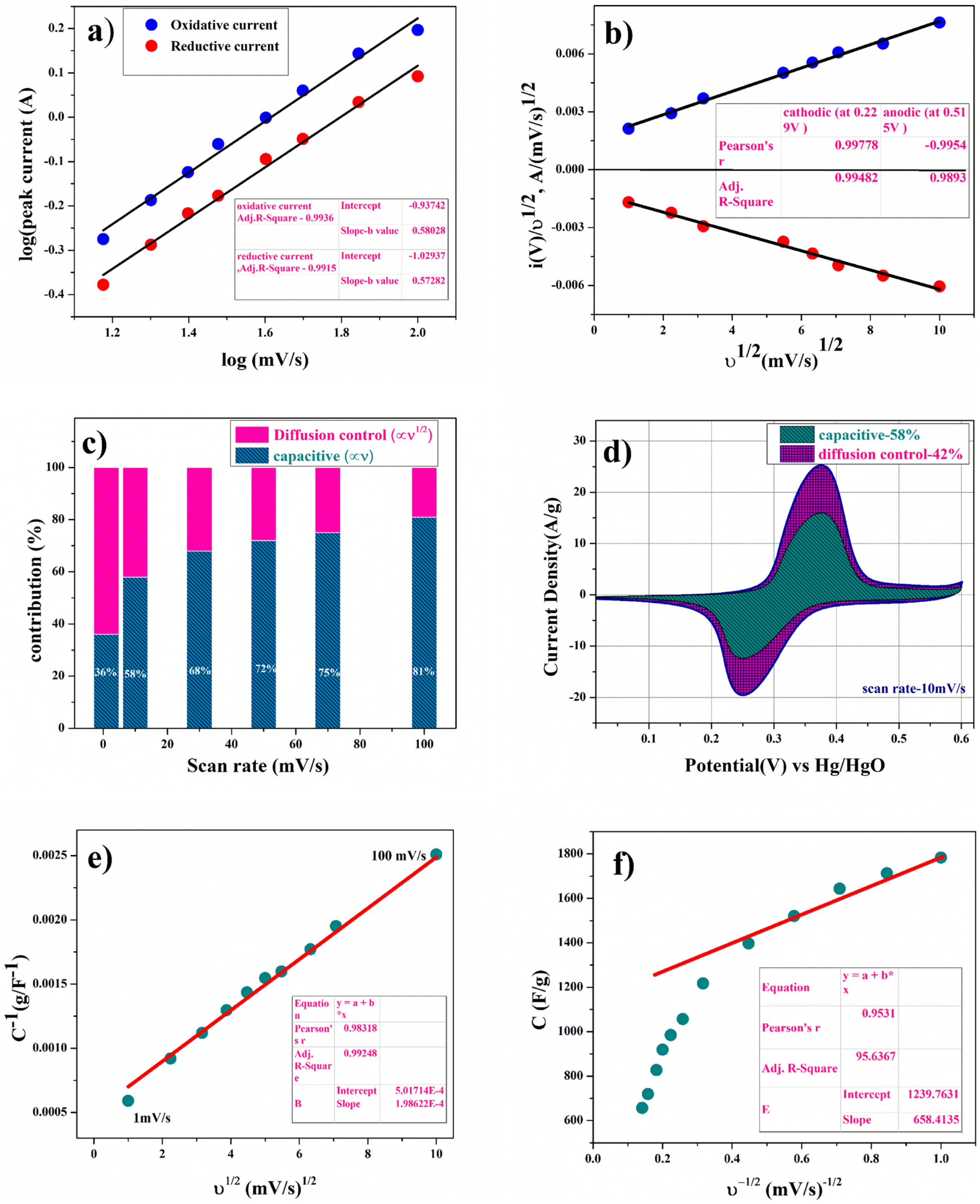

Figure 5. Electrodynamic characteristics of the $Ni_{0.5}Co_{0.5}C_2O_4$ electrode; (a) plot of the linear relationship between log (peak current) and log (scan rate) at two different scan rate regions, (b) plot of power law of the charged state at a potential and discharged state at a potential, (c) contribution of diffusive and capacitive contribution at different scan rates, (d) analysis of kinetic contribution at 10 mV/s, and (e,f) Trasatti plot at different scan rates.

To further estimate qualitative contribution of the different charge storage kinetics/mechanisms of the electrode, the power law equation given in eq 10 was utilized.

$$i = a\nu^b \tag{10}$$

where a and b are adjustable values, i is the current (A), and ν is the scan rate (V/s). The value of b lies between 0.5 and 1, b = 0.5 stands for the semi-infinite diffusion control reaction, that is, battery type intercalative behavior, while b = 1 stands

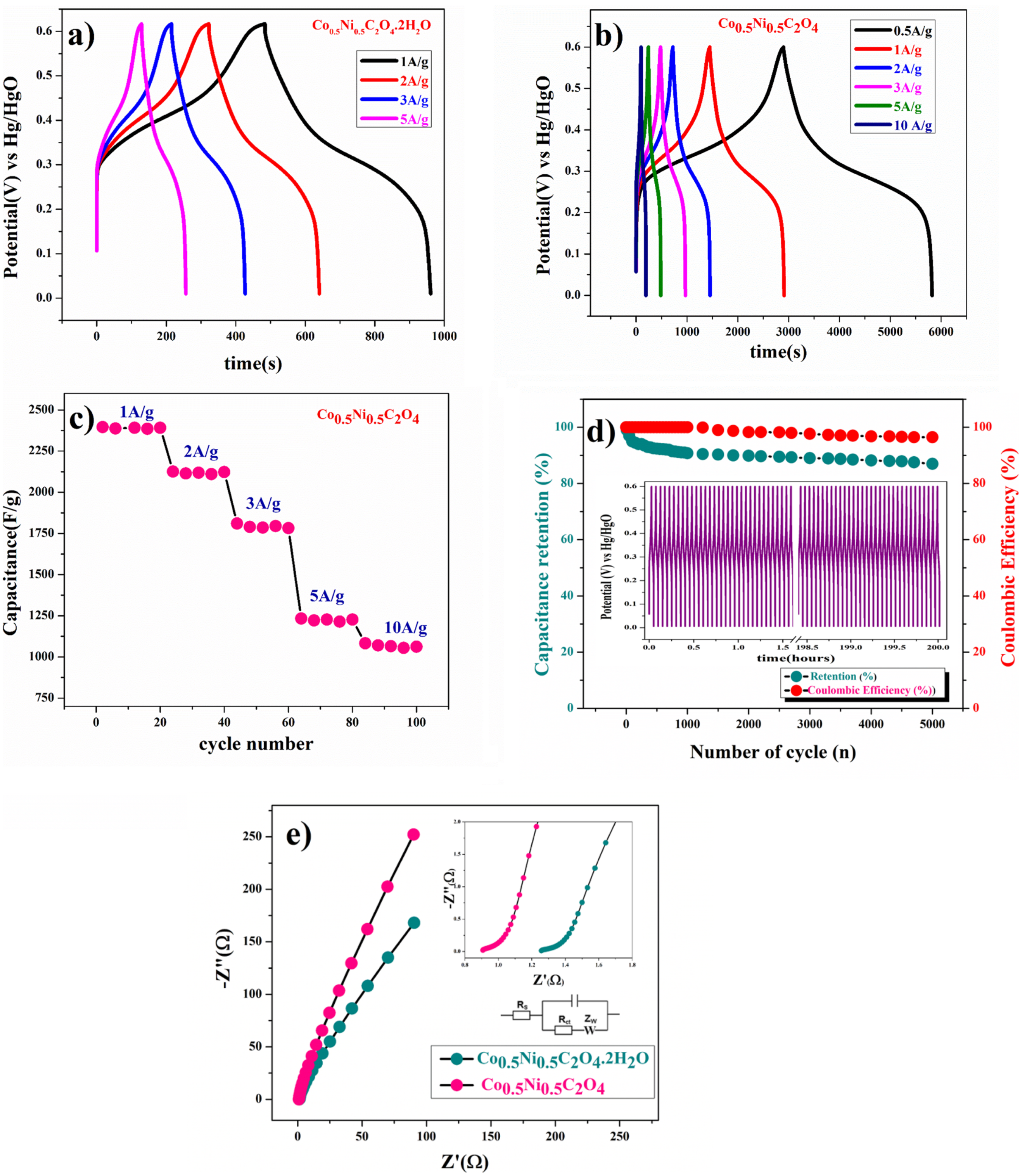

Figure 6. (a) Charge/discharge curve of $Ni_{0.5}Co_{0.5}C_2O_4{\cdot}2H_2O$, (b) charge/charge curve of porous anhydrous $Ni_{0.5}Co_{0.5}C_2O_4$, (c) capacitance performance of porous anhydrous $Ni_{0.5}Co_{0.5}C_2O_4$ at different constant current rates, (d) capacitance retention and Coulombic efficiency porous anhydrous $Ni_{0.5}Co_{0.5}C_2O_4$, and (e) EIS plot and enlarged (zoom) view of the EIS plot of $Ni_{0.5}Co_{0.5}C_2O_4{\cdot}2H_2O$ and porous anhydrous $Ni_{0.5}Co_{0.5}C_2O_4$ electrode at 10 mV (AC).

for the surface control reaction or electrosorption. Figure 5a shows the slopes (b value) of the corresponding log [peak current (i_p) versus log(ν) plots]. The b-values of oxidative and reductive current were found to be 0.58 and 0.57, respectively, indicating the dominance of semi-infinite diffusion-controlled intercalative processes resulting in battery-type supercapacitor behavior during the electrochemical reaction.[35]

Figure 5b shows the voltammetry sweep rate dependence that can distinguish quantitatively the capacitive contribution to the current response. The current response at a fixed

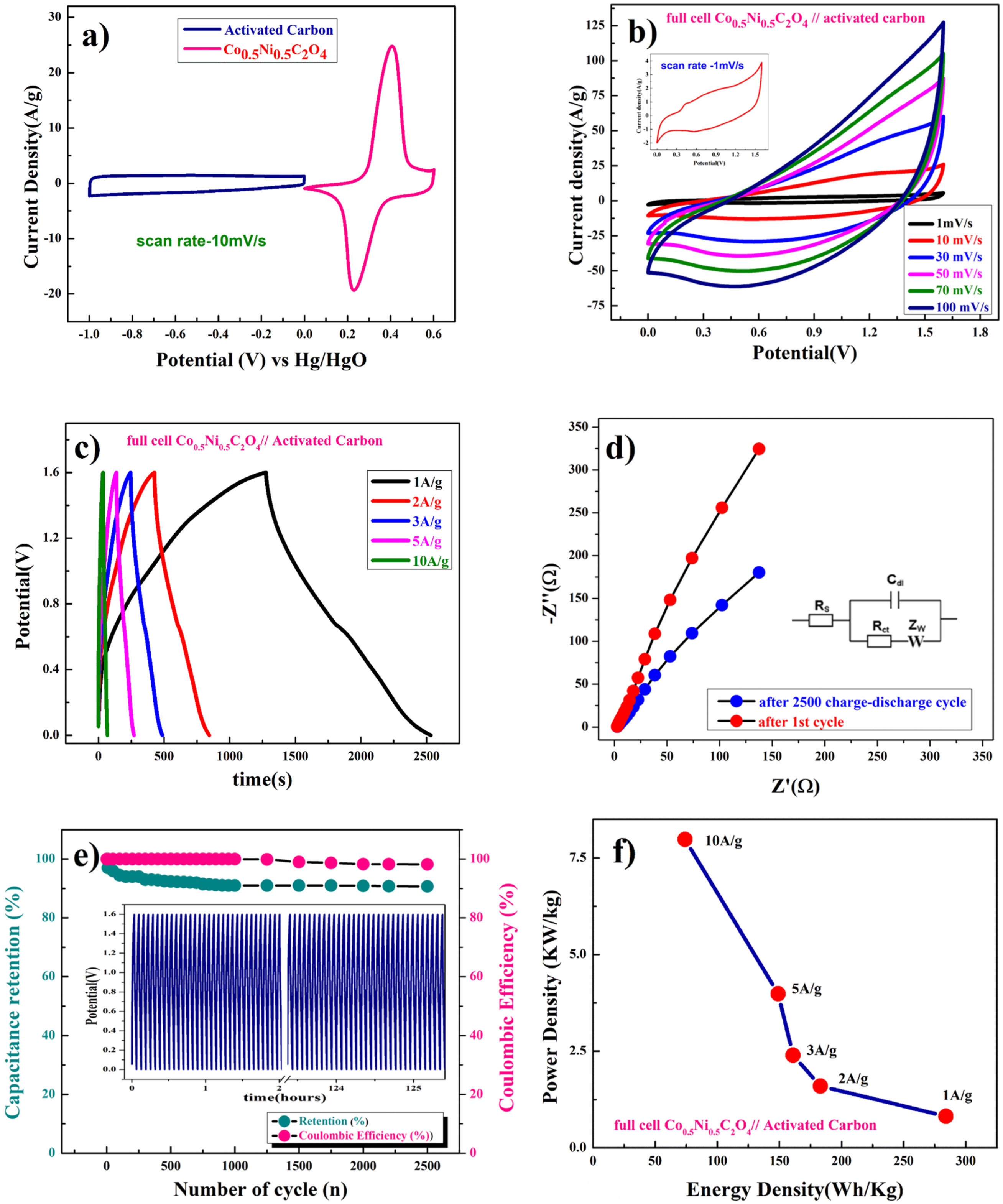

Figure 7. (a) Representative CV for activated carbon (AC) and porous anhydrous $Ni_{0.5}Co_{0.5}C_2O_4$ at 10 mV/s, (b) plot for activated carbon and the porous anhydrous $Ni_{0.5}Co_{0.5}C_2O_4$ cell in ASC mode CV at different scan rates, (c) charge/discharge at different current rates, (d) EIS at 10 mV (AC), (e) capacitance retention and columbic efficiency, and (f) power density and energy density of two electrode cells in ASC mode.

potential is the contribution of two separate mechanisms, surface capacitive effects, and diffusion-controlled insertion or intercalation.

$$i(\upsilon) = k_1\nu + k_2\nu^{1/2} \tag{11}$$

For better understanding, eq 11 was modified as

$$\frac{i(\upsilon)}{\upsilon^{1/2}} = \frac{k_1}{\upsilon^{1/2}} + k_2 \tag{12}$$

In eq 11, $k_1 \upsilon$ and $k_2 \upsilon^{1/2}$ represent the current contributions from the surface capacitive process and the diffusion-controlled intercalation process, respectively. Thus, after determination of k_1 and k_2, we can quantify their contribution in the current density at specific potentials.[36] k_1 and k_2 were determined from obtaining the slope and intercept of y axis from linear fit. The representative curve ($i(V)/\upsilon^{1/2}$ vs $\upsilon^{1/2}$) shown in Figure 5c represents the contribution of surface capacitance and diffusion-controlled intercalatio at different scan rates. Figure 5d represents specific contribution at a 10 mV/s scan rate, and contribution of surface capacitance or electrosorption was found to be 58% and that of diffusion-controlled intercalation was found to be close to 42%.

According to Trassati, the total specific capacitance is the sum of inner and outer surface capacitance of the electrode. It can be expressed as

$$C_{\text{total}} = C_{\text{in}} + C_{\text{out}}\ (\text{F}/\text{g}) \tag{13}$$

The specific capacitance contributed from the inner and outer surface of the electrode is dependent on scan rates.[37] Figure 5e shows the linear fit C^{-1} versus $\upsilon^{1/2}$ at different scan rates, and the y-intercept represents the amount of total charge storage or capacitance of the electrode. Figure 5f shows the linear fit C versus $\upsilon^{-1/2}$, and the y-intercept represents the outer surface charge storage or capacitance of the electrode. After calculating the y-intercept value applied on the Trassati plot, the total capacitance value (C_{total}) was found to be 1993F/g, C_{in} was found to be 754 F/g (38% of the total capacitance value), and C_{out} was found to be 1239 F/g (62% of the total capacitance value).

Galvanostatic experiments were carried out to get more accurate capacity assessment of $Co_{0.5}Ni_{0.5}CO_4{\cdot}2H_2O$ and highly porous anhydrous $Co_{0.5}Ni_{0.5}CO_4$ electrodes. From the charge/discharge curve, the specific capacitance of the electrode was calculated using eq 14.[32]

$$C_{\text{sp}} = \frac{I\Delta t}{m\Delta V} \tag{14}$$

where I is the discharge current (A), Δt is the discharge time (s), m is the mass of the active material in the electrode (g), and ΔV is the potential change during discharge (V). Figure 6a depicts the specific capacitances of $Co_{0.5}Ni_{0.5}C_2O_4{\cdot}2H_2O$, and the values were found to be 810, 350, and 216 F/g at current densities of 1, 2, and 5A/g, respectively. Figure 6b shows the specific capacitances of the highly porous anhydrous $Co_{0.5}Ni_{0.5}C_2O_4$ electrode, and the values were found to be 2409, 2396, 2126, 1226, and 1083 F/g at current densities of 0.5, 1, 2, 5, and 10 A/g, respectively.

It has been observed that with increase in current density, there was decrease in specific capacitance of the electrode. In the desired range of current density, the specific capacitance decreases to 55% of its initial value. Figure 6c shows the capacitance value of the cycle number with different currents of the highly porous anhydrous $Co_{0.5}Ni_{0.5}C_2O_4$ electrode. Figure 6d exhibits the excellent long-term cyclic stability of highly porous anhydrous $Co_{0.5}Ni_{0.5}C_2O_4$ electrodes at 10 A/g for 5000 cycles. 87% capacity retention reflects that the specific capacitance of the electrode did not change much from the initial capacitance after 5000 cycles. The columbic efficiency ($\eta = t_d/t_c$) of the electrode was 94.8% after 5000 cycles of charge/discharge, which reveals the high reversibility of the highly porous anhydrous $Co_{0.5}Ni_{0.5}C_2O_4$ electrode. In addition to electrochemical stability, we performed AC electrochemical impedance spectroscopy (EIS) at 10 mV, as shown in the Nyquist plot in Figure 6e, in the frequency range of 1 MHz to 0.1 Hz. The specific impedance contribution was attributed to the impedance distributions over electric series resistance (R_s), charge transfer resistance (R_{ct}), and Warburg impedance (R_w). Higher frequency resistance was found for $Co_{0.5}Ni_{0.5}C_2O_4{\cdot}2H_2O$ than porous anhydrous $Co_{0.5}Ni_{0.5}C_2O_4$ electrodes, as the intercept of the EIS spectra on the real axis was found to be at 1.43 and 0.8 Ω, respectively, indicating very small internal resistance for the anhydrous $Co_{0.5}Ni_{0.5}C_2O_4$ electrode. The small semicircle in the high frequency region shows the fast charge transport between the electrode and electrolyte. Lower frequency data represent the Warburg diffusion resistance for the samples. The straight line in the low frequency region for the porous anhydrous $Co_{0.5}Ni_{0.5}C_2O_4$ electrode is close to a 90° angle [very close to $-Z''(\Omega)$ axis], and the horizontal line represents the characteristic of more pseudocapacitance behavior of the electrode. The straight line in the low frequency region also represents fast OH− ion diffusion in the porous structure.[38]

Two Electrode Test. To understand the real charge storage behavior of the porous anhydrous $Co_{0.5}Ni_{0.5}C_2O_4$ sample relative to AC (activated carbon), two electrode measurements have been conducted in 2 M KOH. To determine the maximum specific capacitance during the full test, storage capacity of positive and negative electrodes needs to be balanced as per the following equation

$$\frac{1}{C_{\text{total}}} = \frac{1}{C_{\text{positive}}} + \frac{1}{C_{\text{negative}}} \tag{15}$$

For balancing the charge storage capacity of the cell, the mass ratio (m^+/m^-) of positive and negative electrode material was measured using the following equation

$$\frac{m^+}{m^-} = \frac{C_- \times \Delta E_-}{C_+ \times \Delta E_+} \tag{16}$$

m^+, m^-, C_+, C_-, ΔE_+, and ΔE_- are mass, specific capacitance, and potential window of positive and negative electrodes estimated by three-electrode measurement, respectively.[39,40]

Figure 7a shows CV curves at a 10 mV/s scan rate, where AC (activate carbon) was used as the negative electrode and porous anhydrous $Co_{0.5}Ni_{0.5}C_2O_4$ was used as the positive electrode. The calculated mass ratio (m^+/m^-) was found to be 1: 5.3 for the asymmetric cell, and the weight of the active material was measured to be 4.41 mg (excluding the weight of acetylene black and PVDF). Figure 7b demonstrates the CV curve of porous anhydrous $Co_{0.5}Ni_{0.5}C_2O_4$//AC two-electrode ASCs [asymmetry supercapacitor cell at scan rates of 1−100 mV/s in this potential window (1.6 V)]. Figure 7c subsequently shows the galvanostatic charge/discharge curve, and the capacitance values were calculated by eq 13. Capacitance values were found to be 796, 515, 453, 421, and 211F/g at current densities of 1, 2, 3, 5, and 10 A/g, respectively. Figure 7d shows the EIS plot (Nyquist) in the frequency range of 1 MHz to 0.1 Hz at 10 mV/s, confirming the retention of the electronic structure and resistance of the full cell (anhydrous $Co_{0.5}Ni_{0.5}C_2O_4$//AC), as impedance of the material decreases after completion of 2500 cycles compared to the first cycle. Figure 7e shows the columbic efficiency of the two-electrode cell, and the cell has lost only 3% efficiency after completion of 2500 cycles with higher capacity retention (90.7%) of its initial value after 2500 cycles. Specific energy

Table 1

material	morphology	capacitance (F g^{-1})	operating potential (V)	electrolyte	reference
CoC_2O_4	thin sheet	1269 F/g at 6 A/g	0−0.5	6 M KOH	41
$Co_{0.5}Mn_{0.4}Ni_{0.1}C_2O_4 \cdot nH_2O$	micropolyhedrons	990 F/g at 0.6 A/g	0−0.4	3 M KOH	42
$CoC_2O_4 \cdot 2H_2O$	2D porous thin sheets	1.631 F/cm^2 at 1.20 mA/cm	0−0.4	6 M KOH	43
NiC_2O_4	2D thin sheet	2835 F/g at 1 A/g	0−0.4	6 M KOH	44
$Ni_{0.55}Co_{0.45}C_2O_4$	microcuboid	562 F/g at 1 A/g	0−0.6	6 M KOH	29
MnC_2O_4/GO	olive-like	122 F/g at 0.5 A/g	−0.1−0.55	6 M KOH	35
$Co_{0.5}Ni_{0.5}C_2O_4 \cdot 2H_2O$ anhydrous		810 F/g at 1 A/g	0−0.6	2 M KOH	present work
$Co_{0.5}Ni_{0.5}C_2O_4$	nanoflakes	2409 F/g at 1 A/g and 1993 F/g at 1 mV/s	0−0.6	2 M KOH	present work

and specific power of asymmetric capacitors were calculated using the following equations

$$E(\mathrm{W\,h/kg}) = \frac{1}{2}\frac{C_{\mathrm{ASCs}}}{3.6}V^2 \tag{17}$$

$$P(\mathrm{W/kg}) = \frac{E \times 3600}{t_{\mathrm{dis}}} \tag{18}$$

where C_{ASCs} is specific capacitance, V is operating voltage and t_{dis} is discharge time.[40]

Figure 7f shows the plot of specific energy versus specific power with different constant current rates. Resultant values confirm the highest specific energy equivalent to 283 W h/kg at 1 A/g current density with specific power equivalent to ~817 W/kg. The maximum specific power of ~7981 W/kg was obtained when specific energy reduced to ~75.37 W h/kg at 10 A/g of current density. The capacitances of bulk/pristine transition-metal oxalate-based pseudocapacitors are summarized in Table 1 and are similar to those of anhydrous $Co_{0.5}Ni_{0.5}C_2O_4$ electrodes. The charge storage pseudocapacitive behavior of the $Co_{0.5}Ni_{0.5}C_2O_4$ electrode and the capacitance value are comparable or superior to that of most of bulk/pristine transition-metal oxalate-based pseudocapacitors reported to date.[29,41−44] We believe that the control release of the water molecule from hydrated transition oxalate molecule results in anhydrous porous structured material that can accommodate storage of two molecules/ions (OH^-) (intercalation couple with double layer capacitance) over the electrode is the key step in developing superior capacitance or charge storage materials.[45]

■ CONCLUSIONS

In summary, porous anhydrous $Co_{0.5}Ni_{0.5}C_2O_4$ was successfully synthesized using a two-step process; first, $Co_{0.5}Ni_{0.5}C_2O_4 \cdot 2H_2O$ was synthesized by the co-precipitation method in aqueous medium, and then $Co_{0.5}Ni_{0.5}C_2O_4 \cdot 2H_2O$ was heated at 230 °C for 5 h, which resulted in porous anhydrous $Co_{0.5}Ni_{0.5}C_2O_4$. The anhydrous $Co_{0.5}Ni_{0.5}C_2O_4$ electrode showed a highly pseudocapacitive performance with a specific capacitance of 2396 F/g at a current density of 1 A/g and excellent cyclic stability. Predominant intercalative mechanism seems to operative behind high charge storage capacity of the materials as intercalative (inner) and surface (outer) charges stored by porous anhydrous $Co_{0.5}Ni_{0.5}C_2O_4$ were close to high 38 and 62%, respectively. The porous anhydrous $Co_{0.5}Ni_{0.5}C_2O_4$//AC full cell resulted in 283 W h/kg of maximum specific energy with a specific power equivalent to 817 W/kg in the voltage window of 1.6 V in the 2 M KOH electrolyte at a 1 A/g current rate. These results confirm that porous anhydrous $Co_{0.5}Ni_{0.5}C_2O_4$ can act as a potential pseudocapacitive electrode for large-scale energy storage application.

■ AUTHOR INFORMATION

Corresponding Author

Preetam Singh − *Department of Ceramic Engineering, Indian Institute of Technology (Banaras Hindu University), Varanasi, Uttar Pradesh 221005, India;* orcid.org/0000-0002-7590-3576; Phone: 91-9473720659; Email: preetamsingh.cer@itbhu.ac.in, preetamchem@gmail.com

Authors

Neeraj Kumar Mishra − *Department of Ceramic Engineering, Indian Institute of Technology (Banaras Hindu University), Varanasi, Uttar Pradesh 221005, India*

Rakesh Mondal − *Department of Ceramic Engineering, Indian Institute of Technology (Banaras Hindu University), Varanasi, Uttar Pradesh 221005, India*

Thandavarayan Maiyalagan − *Electrochemical Energy Laboratory, Department of Chemistry, SRM Institute of Science and Technology, Kattankulathur, Tamilnadu 603203, India;* orcid.org/0000-0003-3528-3824

Complete contact information is available at: https://pubs.acs.org/10.1021/acsomega.1c05356

Author Contributions

P.S. conceptualized and supervised the work. T.M. supervised the electrochemical studies. R.M. and N.K.M. completed the study, and N.K.M. has organized the manuscript.

Notes

The authors declare no competing financial interest.

■ ACKNOWLEDGMENTS

Authors thank Department of Ceramic Engineering, IIT (BHU), for its facility and support. P.S. thanks Science and Engineering Research Board (SERB), India, for the financial support (project no.: EMR/2016/006840). The authors also thankfully acknowledge the financial support from the Scheme for Promotion of Academic and Research Collaboration (SPARC) of the Ministry of Human Resource Development (MHRD), Government of India, SPARC grant no. SPARC/2018-2019/P1122/SL.

■ REFERENCES

(1) Shafiee, S.; Topal, E. When will fossil fuel reserves be diminished? *Energy Pol.* **2009**, *37*, 181−189.

(2) Xiang, C.; Zhao, X.; Tan, L.; Ye, J.; Wu, S.; Zhang, S.; Sun, L. A solar tube: Efficiently converting sunlight into electricity and heat. *Nano Energy* **2019**, *55*, 269−276.

(3) Augustyn, V.; Simon, P.; Dunn, B. Pseudocapacitive oxide materials for high-rate electrochemical energy storage. *Energy Environ. Sci.* **2014**, *7*, 1597.

(4) (a) Brezesinski, T.; Wang, J.; Tolbert, S. H.; Dunn, B. Ordered mesoporous α-MoO3 with iso-oriented nanocrystalline walls for thin-film pseudocapacitors. *Nat. Mater.* **2010**, *9*, 146−151. (b) Kamila, S.; Mohanty, B.; Samantara, A. K.; Guha, P.; Ghosh, A.; Jena, B.; Satyam, P. V.; Mishra, B. K.; Jena, B. K. Highly Active 2D Layered MoS 2 -rGO Hybrids for Energy Conversion and Storage Applications. *Sci. Rep.* **2017**, *7*, 8378.

(5) Brad, A. J.; Inzelt, G.; Scholz, F. *Electrochemical Dictionary*; Springer Science & Business Media, 2008. (ISBN 978-3-642-29551-5).

(6) Conway, B. E. Transition from "Supercapacitor" to "Battery" Behavior in Electrochemical Energy Storage. *J. Electrochem. Soc.* **1991**, *138*, 1539−1548.

(7) Conway, B. E.; Gileadi, E. Kinetic theory of pseudo-capacitance and electrode reactions at appreciable surface coverage. *Trans. Faraday Soc.* **1962**, *58*, 2493−2509.

(8) Conway, B. E.; Angerstein-Kozlowska, H. The electrochemical study of multiple-state adsorption in monolayers. *Acc. Chem. Res.* **1981**, *14*, 49−56.

(9) Trasatti, S.; Buzzanca, G. Ruthenium dioxide: A new interesting electrode material. Solid state structure and electrochemical behaviour. *J. Electroanal. Chem. Interfacial Electrochem.* **1971**, *29*, A1−A5.

(10) Lee, H. Y.; Goodenough, J. B. Supercapacitor Behavior with KCl Electrolyte. *J. Solid State Chem.* **1999**, *144*, 220−223.

(11) Gogotsi, Y.; Penner, R. M. Energy Storage in Nanomaterials - Capacitive, Pseudocapacitive, or Battery-like? *ACS Nano* **2018**, *12*, 2081−2083.

(12) Costentin, C.; Porter, T. R.; Savéant, J.-M. How Do Pseudocapacitors Store Energy? Theoretical Analysis and Experimental Illustration. *ACS Appl. Mater. Interfaces* **2017**, *9*, 8649−8658.

(13) Dubal, D. P.; Ayyad, O.; Ruiz, V.; Gómez-Romero, P. Hybrid energy storage: the merging of battery and supercapacitor chemistries. *Chem. Soc. Rev.* **2015**, *44*, 1777−1790.

(14) Devaraj, S.; Munichandraiah, N. Effect of Crystallographic Structure of MnO2 on Its Electrochemical Capacitance Properties. *J. Phys. Chem. C* **2008**, *112*, 4406−4417.

(15) Liu, K. C.; Anderson, M. A. Porous Nickel Oxide/Nickel Films for Electrochemical Capacitors. *J. Electrochem. Soc.* **1996**, *143*, 124−130.

(16) (a) Lee, H. Y.; Goodenough, J. B. Ideal Supercapacitor Behavior of Amorphous V2O5·nH2O in Potassium Chloride (KCl) Aqueous Solution. *J. Solid State Chem.* **1999**, *148*, 81−84. (b) Kamila, S.; Mane, P.; Mohanty, R. I.; Chakraborty, B.; Jena, B. K. Supercapacitor properties of V10O14(OH)2 and reduced graphene oxide hybrids: Experimental and theoretical insights. *Electrochim. Acta* **2021**, *399*, 139357. (c) Kamila, S.; Chakraborty, B.; Basu, S.; Jena, B. K. Combined Experimental and Theoretical Insights into Energy Storage Applications of a VO2(D)-Graphene Hybrid. *J. Phys. Chem. C* **2019**, *123*, 24280−24288.

(17) Gao, Y.; Chen, S.; Cao, D.; Wang, G.; Yin, J. Electrochemical capacitance of Co3O4 nanowire arrays supported on nickel foam. *J. Power Sources* **2010**, *195*, 1757−1760.

(18) Xia, X.-H.; Tu, J.-P.; Wang, X.-L.; Gu, C.-D.; Zhao, X.-B. Mesoporous Co3O4 monolayer hollow-sphere array as electrochemical pseudocapacitor material. *Chem. Commun.* **2011**, *47*, 5786−5788.

(19) Wang, S.-Y.; Ho, K.-C.; Kuo, S.-L.; Wu, N.-L. Investigation on Capacitance Mechanisms of Fe[sub 3]O[sub 4] Electrochemical Capacitors. *J. Electrochem. Soc.* **2006**, *153*, A75−A80.

(20) (a) Liu, X. Y.; Zhang, Y. Q.; Xia, X. H.; Shi, S. J.; Lu, Y.; Wang, X. L.; Gu, C. D.; Tu, J. P. Self-assembled porous NiCo2O4 heterostructure array for electrochemical capacitor. *J. Power Sources* **2013**, *239*, 157−163. (b) Samantara, A. K.; Kamila, S.; Ghosh, A.; Jena, B. K. Highly ordered 1D NiCo2O4 nanorods on graphene: An efficient dual-functional hybrid materials for electrochemical energy conversion and storage applications. *Electrochim. Acta* **2018**, *263*, 147−157.

(21) Jabeen, N.; Xia, Q.; Savilov, S. V.; Aldoshin, S. M.; Yu, Y.; Xia, H. Enhanced Pseudocapacitive Performance of α-MnO2 by Cation Preinsertion. *ACS Appl. Mater. Interfaces* **2016**, *8*, 33732−33740.

(22) (a) Singh, A. K.; Jaiswal, P.; Singh, P. A Review on Transition-metal Oxalate Based Electrode for Supercapacitors. *IOP Conf. Ser.: Mater. Sci. Eng.* **2021**, *1166*, 012032. (b) Mishra, N. K.; Mondal, R.; Singh, P. Synthesis, characterizations and electrochemical performances of anhydrous CoC2O4 nanorods for pseudocapacitive energy storage applications. *RSC Adv.* **2021**, *11*, 33926−33937.

(23) (a) Gao, Y.; Wu, J.; Zhang, W.; Tan, Y.; Gao, J.; Zhao, J.; Tang, B. Synthesis of nickel oxalate/zeolitic imidazolate framework-67 (NiC2O4/ZIF-67) as a supercapacitor electrode. *New J. Chem.* **2015**, *39*, 94−97. (b) Zhang, Y.-Z.; Zhao, J.; Xia, J.; Wang, L.; Lai, W.-Y.; Pang, H.; Huang, W. Room temperature synthesis of cobalt-manganese-nickel oxalates micropolyhedrons for high-performance flexible electrochemical energy storage device. *Sci. Rep.* **2015**, *5*, 8536.

(24) Saraf, M.; Rajak, R.; Mobin, S. M. A fascinating multitasking Cu-MOF/rGO hybrid for high performance supercapacitors and highly sensitive and selective electrochemical nitrite sensors. *J. Mater. Chem. A* **2016**, *4*, 16432−16445.

(25) Han, X.; Tao, K.; Wang, D.; Han, L. Design of a porous cobalt sulfide nanosheet array on Ni foam from zeolitic imidazolate frameworks as an advanced electrode for supercapacitors. *Nanoscale* **2018**, *10*, 2735−2741.

(26) Yang, J.; Xiong, P.; Zheng, C.; Qiu, H.; Wei, M. Metal-organic frameworks: a new promising class of materials for a high performance supercapacitor electrode. *J. Mater. Chem. A* **2014**, *2*, 16640−16644.

(27) Wang, J.; Yang, L.; Fu, Y.; Yin, P.; Guan, X.; Wang, G. Delicate control of crystallographic Cu2O derived Ni-Co amorphous double hydroxide nanocages for high-performance hybrid supercapacitors: an experimental and computational investigation. *Nanoscale* **2021**, *13*, 8562−8574.

(28) Małecka, B.; Małecki, A.; Drożdż-Cieśla, E.; Tortet, L.; Llewellyn, P.; Rouquerol, F. Some aspects of thermal decomposition of $NiC_2O_4{\cdot}2H_2O$. *Thermochim. Acta* **2007**, *466*, 57−62.

(29) Wang, L.; Zhang, R.; Jiang, Y.; Tian, H.; Tan, Y.; Zhu, K.; Yu, Z.; Li, W. Interfacial synthesis of micro-cuboid Ni0.55Co0.45C2O4 solid solution with enhanced electrochemical performance for hybrid supercapacitors. *Nanoscale* **2019**, *11*, 13894−13902.

(30) Chenakin, S.; Kruse, N. XPS characterization of transition metal oxalates. *Appl. Surf. Sci.* **2020**, *515*, 146041.

(31) Evanko, B.; Boettcher, S. W.; Yoo, S. J.; Stucky, G. D. Redox-Enhanced Electrochemical Capacitors: Status, Opportunity, and Best Practices for Performance Evaluation. *ACS Energy Lett.* **2017**, *2*, 2581−2590.

(32) Shi, F.; Li, L.; Wang, X.-L.; Gu, C.-D.; Tu, J.-P. Metal oxide/hydroxide-based materials for supercapacitors. *RSC Adv.* **2014**, *4*, 41910−41921.

(33) Jha, M. K.; Babu, B.; Parker, B. J.; Surendran, V.; Cameron, N. R.; Shaijumon, M. M.; Subramaniam, C. Hierarchically engineered nanocarbon florets as bifunctional electrode materials for adsorptive and intercalative energy storage. *ACS Appl. Mater. Interfaces* **2020**, *12*, 42669−42677.

(34) Hanzu, I.; Djenizian, T.; Knauth, P. Electrical and Point Defect Properties of TiO2 Nanotubes Fabricated by Electrochemical Anodization. *J. Phys. Chem. C* **2011**, *115*, 5989−5996.

(35) Augustyn, V.; Come, J.; Lowe, M. A.; Kim, J. W.; Taberna, P.-L.; Tolbert, S. H.; Abruña, H. D.; Simon, P.; Dunn, B. High-rate electrochemical energy storage through Li+ intercalation pseudocapacitance. *Nat. Mater.* **2013**, *12*, 518−522.

(36) Kim, H.-S.; Cook, J. B.; Lin, H.; Ko, J. S.; Tolbert, S. H.; Ozolins, V.; Dunn, B. Oxygen vacancies enhance pseudocapacitive charge storage properties of MoO3−x. *Nat. Mater.* **2017**, *16*, 454−460.

(37) Ren, W.; Chen, X.; Zhao, C. Ultrafast Aqueous Potassium-Ion Batteries Cathode for Stable Intermittent Grid-Scale Energy Storage. *Adv. Energy Mater.* **2018**, *8*, 1801413.

(38) Basiricò, L.; Lanzara, G. Moving towards high-power, high-frequency and low-resistance CNT supercapacitors by tuning the CNT length, axial deformation and contact resistance. *Nanotechnology* **2012**, *23*, 305401.

(39) Subramani, K.; Sudhan, N.; Divya, R.; Sathish, M. All-solid-state asymmetric supercapacitors based on cobalt hexacyanoferrate-derived CoS and activated carbon. *RSC Adv.* **2017**, *7*, 6648−6659.

(40) Hu, N.; Gong, W. H.; Huang, L.; Shen, P. K. Ultrahigh energy density asymmetric electrochemical capacitors based on flower-like ZnO/Co3O4 nanobundle arrays and stereotaxically constricted graphene. *J. Mater. Chem. A* **2019**, *7*, 1273−1280.

(41) Cheng, G.; Si, C.; Zhang, J.; Wang, Y.; Yang, W.; Dong, C.; Zhang, Z. Facile fabrication of cobalt oxalate nanostructures with superior specific capacitance and super-long cycling stability. *J. Power Sources* **2016**, *312*, 184−191.

(42) Zhang, Y.-Z.; Zhao, J.; Xia, J.; Wang, L.; Lai, W.-Y.; Pang, H.; Huang, W. Room temperature synthesis of cobalt-manganese-nickel oxalates micropolyhedrons for high-performance flexible electrochemical energy storage device. *Sci. Rep.* **2015**, *5*, 8536.

(43) Pu, T.; Li, J.; Jiang, Y.; Huang, B.; Wang, W.; Zhao, C.; Xie, L.; Chen, L. Size and crystallinity control of two-dimensional porous cobalt oxalate thin sheets: tuning surface structure with enhanced performance for aqueous asymmetric supercapacitors. *Dalton Trans.* **2018**, *47*, 9241.

(44) Zhao, C.; Jiang, Y.; Liang, S.; Gao, F.; Xie, L.; Chen, L. Two-dimensional porous nickel oxalate thin sheets constructed by ultrathin nanosheets as electrode materials for high-performance aqueous supercapacitors. *CrystEngComm* **2020**, *22*, 2953.

(45) Liu, T.; Shao, G.; Ji, M.; Ma, Z. Composites of olive-like manganese oxalate on graphene sheets for supercapacitor electrodes. *Ionics* **2014**, *20*, 145−149.

https://doi.org/10.1021/acsomega.1c05356